

Analytical modeling of work hardening of duplex steel alloys in milling process

yousef mohammadi (✉ yousefmohammadi13@yahoo.com)

University of Birjand

Hossein Amirabadi

University of Birjand, University of Neyshabur

Research Article

Keywords: Work Hardening, Duplex Stainless Steel, Side Milling, Strain Hardening

Posted Date: March 23rd, 2021

DOI: <https://doi.org/10.21203/rs.3.rs-293890/v1>

License:   This work is licensed under a Creative Commons Attribution 4.0 International License.

[Read Full License](#)

Version of Record: A version of this preprint was published at Journal of Mechanical Science and Technology on March 3rd, 2022. See the published version at <https://doi.org/10.1007/s12206-022-0231-6>.

Analytical modeling of work hardening of duplex steel alloys in milling process

Yousef Mohammadi¹, Hossein Amirabadi^{1,2,*}

1-Department of Mechanical Engineering, University of Birjand, Birjand,

2- Department of Electrical Engineering, University of Neyshabur, Neyshabur, Iran

* Corresponding author. ORCID ID: 000-0002-5426-4293, E-mail address: hamirabadi@neyshabur.ac.ir

Abstract

Sever plastic deformation in cutting operations such as milling, might change mechanical properties of the machined surface. This study presents an analytical model to calculate work hardening of the upper layers of the workpiece in the milling process of 2205 duplex stainless steel. In this regards, the stresses in the cutting regions are calculated to find the stress and temperature fields in the workpiece. Then the strain and strain rate values are calculated for each point of the surface and subsurface layers using the determined stress field. Finally, Johnson-Cook material model is used to calculate flow stress and work hardening. Experimental results of the different machining conditions has been used to validating the proposed model, however comparisons of subsurface microhardness obtained by analytical model with experimental tests shown that the model properly predicts the amount of work hardening.

Keywords: Work Hardening, Duplex Stainless Steel, Side Milling, Strain Hardening

NOMENCLATURE

A	Yield strength in Johnson-Cook model (MPa)	$\dot{\epsilon}_0$	Reference strain-rate in Johnson-Cook model
B	Strength coefficient in Johnson-Cook model (MPa)	β	Heat partition ratio
C	Strain-rate constant in Johnson-Cook model	τ_{SN}	Shear stress along the SN-line
$\angle IS, \angle SN$	Angle between negative direction of the X-axis and the slip lines, IS and SN (deg)	ϕ_{AB}	Angle between negative direction of the X-axis and the slip line(AB)
C_p	Specific heat (J/kg°C)	ϵ_{AB}	Equivalent strain at AB
K	Thermal conductivity (W/m°C)	$\dot{\epsilon}_{AB}$	Equivalent strain-rate at AB (S^{-1})
V, V_s, V_c	Cutting velocity, Shear velocity, Chip velocity	ζ_1	Friction angle (deg)
P_A, P_B, P_S, P_N	Hydrostatic stresses at the points A, B, S,N	θ_s	Stagnation angle (deg)
C_0	Strain rate constant proposed by Oxley	α	Rake angle. (deg)
K_0	Second-order correction to the Bessel function	ρ	Density (kg/m ³)
T_M	Melting temperature of the work material (°C)	φ_{ij}	Angle of deviation of slip-line ij with respect to the positive direction of the X'-axis (Fig. 6),
T_{AB}	Average temperature along AB (°C)	σ_{AB}	Effective flow stress at AB
T_W	Initial work material temperature (°C)		
a	Thermal diffusivity		

1. Introduction

In cutting operations, because of large amount of mechanical and thermal loads upon surface and subsurface layers, severe plastic deformation occur in these regions. The most important effects of these deformations are the strain hardening of the surface layers. Since these plastic deformations affect the service life of the final product, various researches have been conducted in this field [1-12], in these studies, the effects of machining parameters on strain hardening in the surface layers of the machined workpiece has been investigated experimentally and theoretically.

In some materials, work hardening adversely affects the machining process, and consequently, the temperature and machining forces increase during the cutting operation. This is because an increase in the cutting force increases the tool wear and reduces its life [13-14]. The strain generated on the machined surface and the subsurface layers affects the workpiece microstructure. Therefore, the evaluation of work hardening (strain hardening) on the machined surface and the subsurface layers is necessary and very important. Only a few analytical studies have focused on work hardening and deformations in machining processes, while there are many empirical studies on this issue. The easiest way to determine the plastic deformation is the direct observation of deformed grains, so the effect of machining parameters on materials can be examined. Mike Olsson et al [15] used metallographic and deformation depth analyses on the workpiece surface and subsurface layers to measure the effects (thickness and deformation) of machining process. The limitation of direct observation is the low accuracy in detecting severe plastic deformations in layers near to the machined surface. To cope with this shortage, Bailey and Jeelani [16] used the micro-grid method to evaluate distorted grids specified on the workpiece. Ghadbeigi et al [17] printed microgrids with a pitch of 10 μ m and a line width of less than 1 μ m on work surface to detect micro-scale strain. Because printing the microgrids is a very complex process, and the printed microgrids cannot generally withstand the high temperatures during machining, so it is difficult and sometimes impossible to use this technique.

Image correlation techniques are other experimental methods that are used to study the relationship between cutting parameters and plastic deformation of machined surface layers. Guo and M'Saoubi [18] used an image correlation technique to experimentally study the deformation history on the machined surface of copper and brass alloys. Moreover, they controlled the deformation on the machined surface by manipulating the machining parameters. However, experimental techniques of surface deformation monitoring are expensive and time consuming. Therefore, analytical and numerical models are necessary to evaluate the depth and amount of deformation on the machined surface. In the present study, an analytical model is presented to evaluate work hardening in a milling process. Furthermore, it is assumed that in the milling process, the machined surface and the subsurface layers at any point undergo several times plastic deformation before the cutter reaches the point. Consequently, a workpiece element (on the surface and near-surface layers) is subjected to change in its mechanical properties (from the first moment) until the cutter passes through it. In the proposed model, these changes are considered, and the hardness curve at each point of the workpiece surface in the inward direction is finally calculated and evaluated.

2. Calculating stresses on the surface layers

There are two zones of mechanical load on the workpiece in the cutting process, as shown in Fig. 1. Mechanical load due to Contact between the cutting edge and the workpiece in the primary and tertiary zones results in normal and shear stresses on the workpiece [19].

The combination of the parallel-sided shear plane model proposed by Oxley and Young[20] and the slip line field on the cutting tool edge proposed by Fang [21, 22] was used in the present study to calculate the stresses in the orthogonal cutting process and to describe the cutting zones, and it is illustrated in Fig. 2. The primary shear zone is considered as the region between two parallel sides. Normal and tangential stresses act along slip-lines AB, BI, IS and SN, which are almost in the middle of this region. In Fig. 2, F is intersection point between the rake face and the cutting tool edge, N is intersection point between the machined

In side milling, the orthogonal cutting condition is satisfied when the cutting edges are parallel to the tool holder axis and the tool feeds along the X axis as shown in Fig. 3.

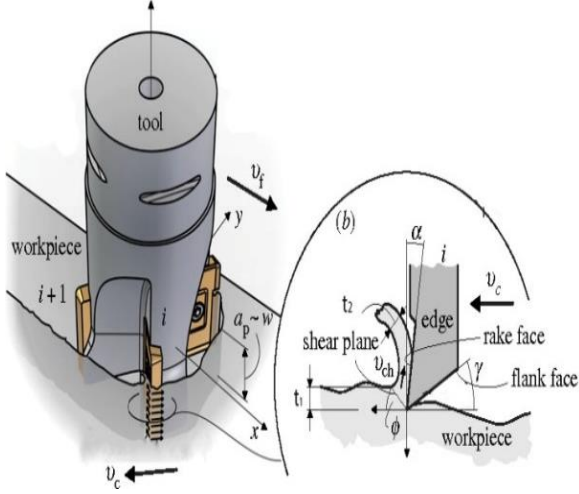


Fig. 3 Geometric parameters of orthogonal cutting in milling.

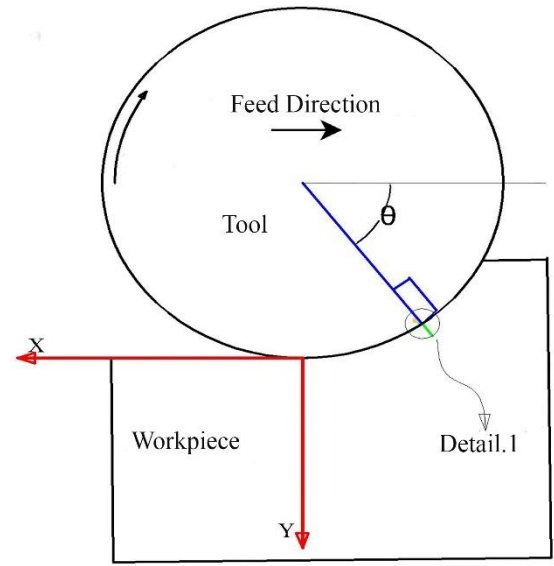
Fig.4 shows a milling process in which each angle of tool-workpiece interaction around the cutting edge conforms to the slip-line model. According to the model proposed by Zhang[25], the stresses along the slip-lines AB, BI, IS and SN are applied to the workpiece as shown in Fig. 4c. During the cutting process, the element M of the workpiece in a subsurface layer near the machined surface has to pass at the cutting speed through a thermo-mechanical stress field. This element undergoes deformation and distortion due to high stress along the path specified in Fig. 4c. Therefore, the stresses from various sources (slip-lines) on this element are calculated separately at each point of the path. These stresses are finally summed up [26]. The distributions of shear and hydrostatic stresses on each slip-line can be used to calculate the stress field in the workpiece by Boussinesq equations[27] (Eqs. 8-10) as shown in Fig. 5.

$$\sigma_x = -\frac{2z}{\pi} \int_{-b}^a \frac{P(s)(x-s)^2}{[(x-s)^2+z^2]^2} ds - \frac{2}{\pi} \int_{-b}^a \frac{q(s)(x-s)^3}{[(x-s)^2+z^2]^2} ds \quad (8)$$

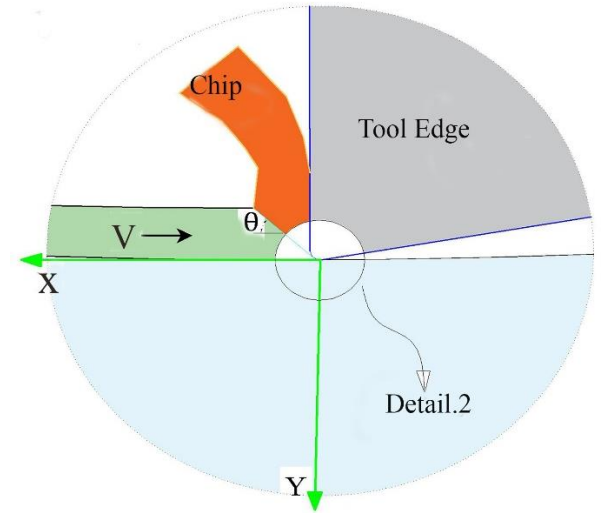
$$\sigma_z = -\frac{2z^3}{\pi} \int_{-b}^a \frac{P(s)}{[(x-s)^2+z^2]^2} ds - \frac{2z^2}{\pi} \int_{-b}^a \frac{q(s)(x-s)}{[(x-s)^2+z^2]^2} ds \quad (9)$$

$$\tau_{xz} = -\frac{2z^2}{\pi} \int_{-b}^a \frac{P(s)(x-s)}{[(x-s)^2+z^2]^2} ds - \frac{2z}{\pi} \int_{-b}^a \frac{q(s)(x-s)^2}{[(x-s)^2+z^2]^2} ds \quad (10)$$

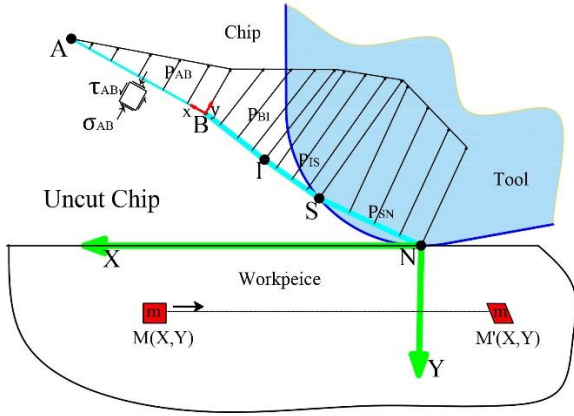
Where $q(s)$ is the distribution of shear stress and $P(s)$ is the distribution of normal stress on each slip-line. Fig.5 shows the parameters used in Boussinesq equations. From Eq. 3 to Eq. 7 and assuming a linear distribution for the normal stress on the slip-lines, the normal stress distributions for AB, BI, IS and SN are calculated from Eqs. 11 to 14, respectively.



a)



b)



c) **Fig. 4** a) An overall view of tool and workpiece and their relative motion, b) Details of interface between cutting edge and workpiece c) details of the cutting zone around the cutting edge and the slip-line model.

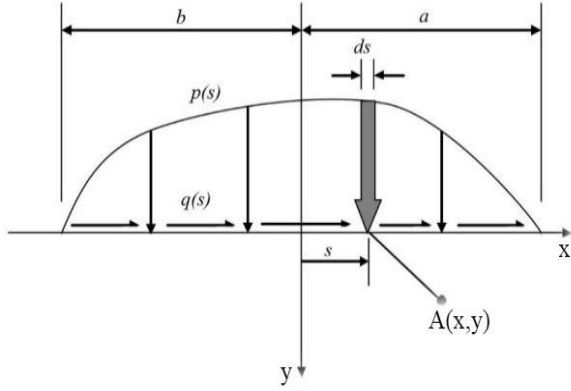


Fig. 5 Boundary conditions for Boussinesq equations [27]

From Eq. 3 to Eq. 7 and assuming a linear distribution for the normal stress on the slip-lines, the normal stress distributions for AB, BI, IS and SN are calculated from Eqs. 11 to 14, respectively.

$$P_{AB} = P_B + \frac{(P_A - P_B)}{l_{AB}} \times s \quad (11)$$

$$P_{BI} = P_I + \frac{(P_B - P_I)}{l_{BI}} \times s \quad (12)$$

$$P_{IS} = P_S + \frac{(P_I - P_S)}{l_{IS}} \times s \quad (13)$$

$$P_{SN} = P_N + \frac{(P_S - P_N)}{l_{SN}} \times s \quad (14)$$

where l_j is the length of slip-line j (j represents AB, BI, IS or SN). Boussinesq equations can be used for each slip-line in the coordinate system $x y_j$. As an example, for slip-line AB, The origin of the coordinate system coincides with point B and the x_{AB} axis lies on slip-line AB directed

toward point A; the y_{AB} axis is in line with the load P_{AB} . The same procedure is considered for other line with the corresponding coordinate systems (Fig. 4c). Therefore, Boussinesq equations for calculating σ_{xx}^j , σ_{yy}^j and τ_{xy}^j (of slip-line j) can be written as Eqs. 15 to 17.

$$\sigma_{xx}^j = -\frac{2y}{\pi} \int_0^{l_j} \frac{P_j(x-s)^2}{[(x-s)^2 + y^2]^2} ds - \frac{2}{\pi} \int_{-b}^{l_j} \frac{\tau_j(x-s)^3}{[(x-s)^2 + y^2]^2} ds \quad (15)$$

$$\sigma_{yy}^j = -\frac{2y^3}{\pi} \int_0^{l_j} \frac{P_j}{[(x-s)^2 + y^2]^2} ds - \frac{2y^2}{\pi} \int_0^{l_j} \frac{\tau_j(x-s)}{[(x-s)^2 + y^2]^2} ds \quad (16)$$

$$\tau_{xy}^{AB} = -\frac{2y^2}{\pi} \int_0^{l_j} \frac{P_j(x-s)}{[(x-s)^2 + y^2]^2} ds - \frac{2y}{\pi} \int_0^{l_j} \frac{\tau_j(x-s)^2}{[(x-s)^2 + y^2]^2} ds \quad (17)$$

therefore, the stress at any point in the workpiece can be calculated from the stresses σ_{xx}^j , σ_{yy}^j and τ_{xy}^j in the coordinate system XY using the coordinate transformation of Eq. 18 and substituting the coordinates in Eqs. 15 to 17. The origin of the coordinate system XY coincides with N (the tip of the tool cutting edge), its X axis is aligned with the cutting speed but in the opposite direction and the Y axis, which is along the line connecting the cutting edge tip to the tool center, is directed into the workpiece (Fig. 4c). In Eq. 18, the coordinate transformation of slip-line AB is illustrated. The same procedure is used for other slip-lines.

$$\begin{bmatrix} x \\ y \end{bmatrix} = \begin{bmatrix} X_B \\ Y_B \end{bmatrix} + \begin{bmatrix} \cos \phi_{AB} & \sin \phi_{AB} \\ -\sin \phi_{AB} & \cos \phi_{AB} \end{bmatrix} \begin{bmatrix} X \\ Y \end{bmatrix} \quad (18)$$

Where ϕ_{AB} is the angle between slip-line AB and the positive direction of the X axis.

2. 3. Temperature field

Temperature directly affects on the variables such as strength, strains and stresses. An analytical modeling of steady state temperature field in metal cutting presented by Hahn [28]. Komanduri and Hou [29] modified the coordinate system of Hahn's solution for an oblique band heat source in a semi-infinite medium, where the non-

machine surface and the chip surface are the boundaries of a semi-infinite medium as shown in Fig. 6. The non-machined surface of the workpiece is assumed to be isolated from the moving heat source. To experience adiabatic conditions on the workpiece boundaries, image heat sources are considered (Fig. 6). In this study, used model that proposed by Karas [30], it is assumed that the heat on the tool-chip interface is fully dissipated by the chip, and no heat is transferred to the workpiece, so the total heat in the workpiece is generated by four oblique heat sources. The first source corresponds to the AB plate, while the second and third sources are related to

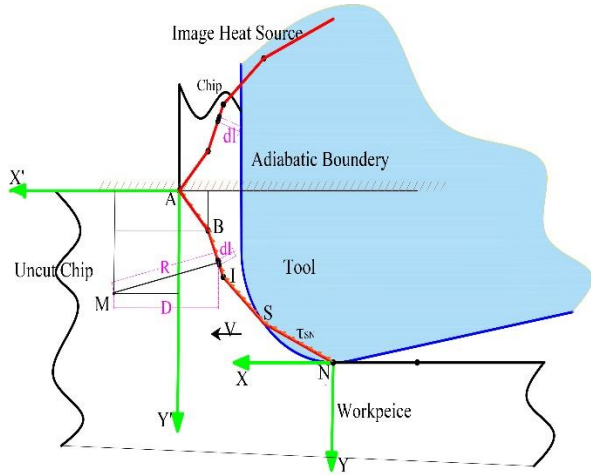


Fig. 6 Heat sources and coordinate axes for calculating temperature.

cutting along slip-lines BI and IS. The fourth heat source is the tool-workpiece friction at their interface along SN. The increase in temperature due to each oblique moving heat source can be calculated from Eq. 19 by considering an image heat source in $X'Y'$ coordinate system.

$$\Delta T_M = \frac{\beta \tau_{ij}}{2\pi\lambda} \int_{l=0}^{L_{ij}} \exp\left(-\left(X'_i + l \cos \varphi_{ij}\right) \frac{V_c}{2a}\right) \left[K_0 \left(\frac{RV_c}{2a} \right) + K_0 \left(\frac{R'V_c}{2a} \right) \right] dl \quad (19)$$

Where ij indicates slip-lines AB, BI, IS and SN, i which conforms to ij , corresponds to points A, B, I and S, respectively. For example, L_{AB} is the length of the slip-line AB and X'_A is the coordinate of point A on the X' axis; t denotes the tool material and V is the shear velocity; K is the heat conductivity coefficient and a is thermal diffusivity, which satisfy the relation $a = k/\rho C_p$; K_0 is the second-order correction to the Bessel function, φ_{ij} is the angle of deviation of slip-line ij with respect to the positive direction of the X' axis (Fig.6), q_{ij} is the heat flux defined as $q_{ij} = \tau_{ij} V_{ij}$ (where τ_{ij} and V_{ij} are, respectively, the shear stress along slip-line ij and the

relative shear velocity along this line. It is assumed that the shear velocity of the three moving heat sources BI, IS and SN is equal to the shear velocity for the heat source moving along AB, i.e., the same as V_s .

Additionally, R is the distance from M to the element dl on slip-line ij and R' is the distance from M to the element dl on the image of slip line ij . These values are calculated from the Eqs. 20 and 21.

$$R_{ij} = \sqrt{(X'_M - X'_i - l \cos \varphi_{ij})^2 + (Y'_M - Y'_i - l \sin \varphi_{ij})^2} \quad (20)$$

$$R'_{ij} = \sqrt{(X'_M - X'_i - l \cos \varphi_{ij})^2 + (Y'_M + Y'_i + l \sin \varphi_{ij})^2} \quad (21)$$

The heat partition ratio, β , is calculated from Eq. 22 for slip-line AB, BI and IS from Eq. 22, while this parameter is calculated from Eq. 23 for the heat source SN.

$$\beta = \begin{cases} 0.5 - 0.35 \log(R_T \tan \phi) & 0.04 \leq R_T \tan \phi \leq 10 \\ 0.3 - 0.15 \log(R_T \tan \phi) & R_T \tan \phi > 10 \end{cases} \quad (22)$$

$$\beta = \sqrt{K\rho C_p} / (\sqrt{K\rho C_p} + \sqrt{K^t \rho^t C_p^t}) \quad (23)$$

The temperature rise at any point of M in the workpiece, caused by the all heat source. Therefore, the final temperature at point M of the workpiece is obtained by Eq. 24.

$$T_M = T_0 + \Delta T_{M-tot} = T_0 + \Delta T_{AB} + \Delta T_{BI} + \Delta T_{IS} + \Delta T_{SN} \quad (24)$$

2. 4. Calculating strains on the surface layers

The strains in the region of the workpiece that is subjected to a combination of elastic and plastic deformations can be calculated from normal and shear stress applied to each element in this region. These values can then be used along with the Von Mises criterion to obtain the effective stress applied to the elements via Eq. 25 [31]

$$\sigma_i^e = \frac{1}{\sqrt{2}} [(\sigma_{11}^e - \sigma_{22}^e)^2 + (\sigma_{11}^e - \sigma_{33}^e)^2 + (\sigma_{22}^e - \sigma_{33}^e)^2]^{1/2} \quad (25)$$

Where σ_{ii}^e denote the principal stresses. Using Hook's law the equivalent elastic strain (ε_i^e) can be calculated as follows:

$$\varepsilon_i^e = \frac{\sigma_i^e}{E} \quad (26)$$

In the plastic phase, the equivalent stress of the material exceeds the yield stress, and a severe plastic deformation occurs in this situation, so analytical modeling of deformation in the elastic-plastic phase is very difficult. In the present study, a simple analytical approach similar to the method implemented in Ref. [31] is used. Based on the elastic theory, when the workpiece material is

subjected to thermo-mechanical fields, the elastic-plastic strain can be obtained as follows:

$$\varepsilon_i^p = \begin{cases} \varepsilon_i^e & \varepsilon_i^e \leq \varepsilon_s \\ \varepsilon_s + \alpha(\varepsilon_i^e - \varepsilon_s) & \varepsilon_i^e > \varepsilon_s \end{cases} \quad (27)$$

where ε_i^p is the strain at point M, ε_s is the strain related to the yield stress σ_s and α is the ratio of plastic to elastic deformation. To obtain α , it is assumed that its value at each point is equal to the ratio of the plastic strain in the subsurface layers to the elastic strain at the same point, i.e., $\alpha = \frac{\varepsilon_T^p}{\varepsilon_s}$.

2. 5. Calculating strain rate

As shown in Fig. 4c, when the element m is displaced by the distance Δx from M to M' (M is the point at which, for the first time, the stress applied to the element m, is greater than its yield stress and M' is the point at which the stress field is smaller than the yield stress of the element m), a plastic strain (ε_T^p) acts on it. If the time of displacement is equal to t , the strain rate is calculated as follows:

$$\dot{\varepsilon}_T^p = \frac{\varepsilon_T^p}{t} \quad (28)$$

$$t = \frac{\Delta x}{V} \quad (29)$$

Where V is the cutting speed.

2. 6. Calculating strength (flow stress)

Using Johnson-Cook model and the values of strain, strain rate and temperature, the strength at any point of $M(X, Y)$ in machined subsurface layers can be calculated from Eq. 30.

$$\sigma_i^s = (\sigma_y^s(X, Y) + B\varepsilon_i^p(X, Y)) \left(1 + C \ln \frac{\dot{\varepsilon}_T^p(X, Y)}{\dot{\varepsilon}_0} \right) \left(1 - \left(\frac{T(X, Y) - T_0}{T_m - T_0} \right)^m \right) \quad (30)$$

Where σ_y^s and T_0 are yield strength and temperature, in point M before cutting, ε_i^p , $\dot{\varepsilon}_T^p$, T are strain, strain rate and temperature in point M during cutting (machining), respectively.

3. Modeling of work hardening profile in milling

In side milling process, when the cutting edges are parallel to the cutting tool axis (Fig. 3), therefore, the orthogonal cut is realized at any angle of engagement of the cutting edge with the workpiece (θ). As a result, the equations in the previous sections can be used to describe the stress and temperature fields at the cutting regions.

In milling process, every point of the machined surface experiences several times plastic deformation. it is assumed that when the tool center is at O_1 and the cutting edge moves along $B'A'$, point A on the workpiece surface undergoes plastic deformation for the first time (shown in the Fig.7). Therefore, the tool cutting edge reaches point A when tool center is displaced by $A'A$, as the tool center gets closer to A (in the direction of tool feed) the intensity of plastic deformation increases. Since the tool center moves by f (feed per tooth), so point A experiences n times plastic deformation until the cutting edge reaches this point. The value of n is calculated from Eq. 31.

$$n = (R + z_{\theta_1}) \cos \theta_{1th} / f \quad (31)$$

Where f is the feed per tooth, R is the radius of the cutter and θ_{1th} is the angle at which point A (any given point on the machined surface) undergoes plastic deformation or strain hardening for the first time. In other words, at θ_{1th} , the penetration depth profile (path BA in Fig. 7) intersects the hypothetical surface that is to be machined (point A). The cold working penetration depth at any rotation angle θ is obtained by equating the flow stress (Eq. 30) with the initial yield strength of the workpiece material. For example z_{θ_1} ($O'A$ in Fig. 7) is penetration depth at θ_{1th} .

In Fig.7, A, can be any point on the uncut surface, so the work hardening at this point can be generalized to the entire machined surface. As discussed for Fig. 7, n cuts (by teeth) are needed for the tool center to move from O_1 and reach point A. Therefore, for each cutting

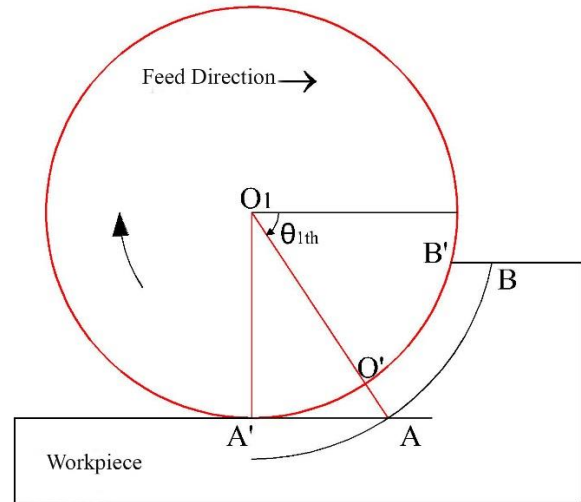
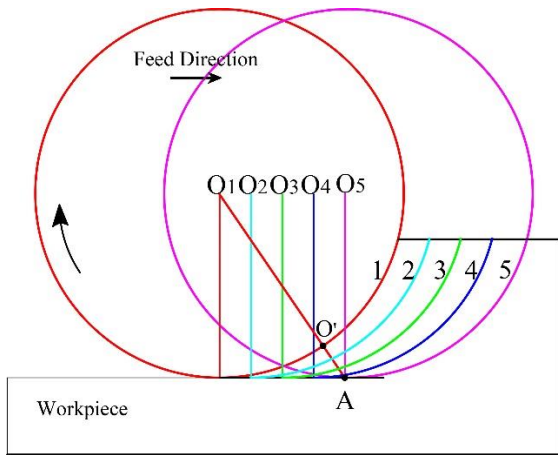
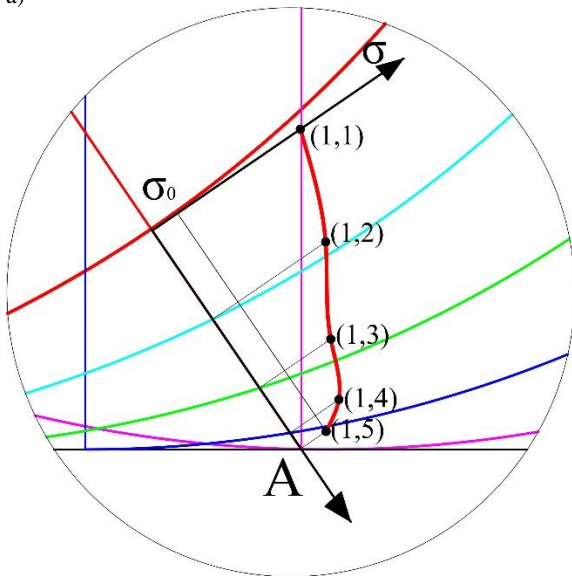


Fig.7 Tool-workpiece engagement and the penetration depth profile of work hardening.



a)



b)

Fig. 8 Cutting paths for a workpiece surface under 5 times deformation and b) details of the edge tip and strength curve.

path k , the surface and subsurface layers have already been deformed plastically in paths 1 to k and their cutting strengths have changed.

Therefore, to obtain the final strength curve (on the machined surface and subsurface layers), the contribution of each cutting path must be included.

Fig.8 shows a milling process with $n = 5$; that is, each point of the uncut surface undergoes 5 times plastic deformation. As the cutting edge moves through path 1, the workpiece strength curve follows O_1A (red curve in Fig. 8b). The second cutting edge cuts path 2, which has already been subjected to work hardening due to cutting through path 1 and has been affected by the strength curve 1. The final yield strength curve (the strength curve of

path 5 at point A) is plotted in Fig. 9 using the contribution of 4 previous paths connecting the tool center to point A. Accordingly, Fig. 9, which is based on the process in Fig. 8, shows 5 strength curves, each consisting of 5 points with (i,j) , where i represents the curve number and j the point number). Using the algorithm in Fig. 10 for each curve, the strength at each point is calculated. This process continues until the final strength curve (number 5) is calculated. Each cutting path has its own strength curve, which is affected by the strength curves of previous paths.

in the algorithm that shown in figure 10, by considering the machining parameter, the number of steps that any point on the machined surface undergoes plastic deformation (n) calculated, then for each step (cutting path), stress and temperature fields are calculated and using these fields, the strength at different depths of the machined path was calculated. In this algorithm $\sigma_{ef}(i)$ is the stress field resulting from the i cutting path, $ZH(i)$ is penetration depth of plastic deformation in i step, $z(i,j)$ is the distance of point j from the machined surface in step i and $\varepsilon(i,j), \dot{\varepsilon}(i,j), T(i,j)$ are strain, strain rate, temperature, respectively for this point.

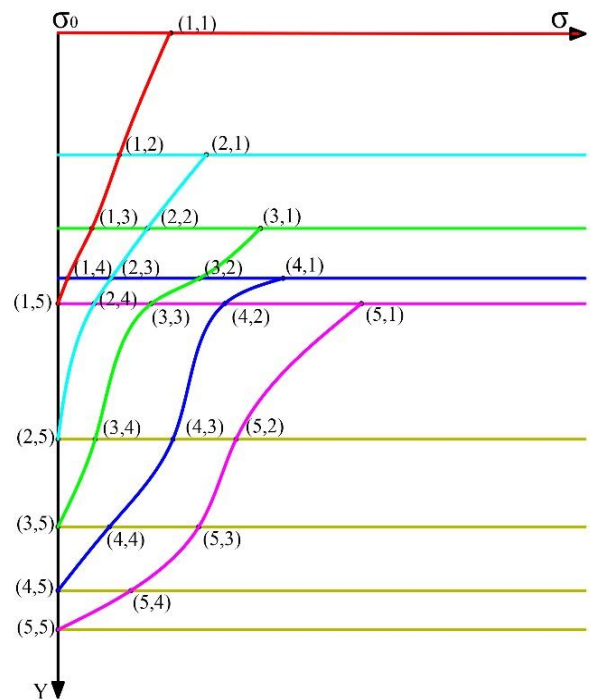


Fig. 9 Schematic of strength curves for cutting paths has been shown in Fig. 8.

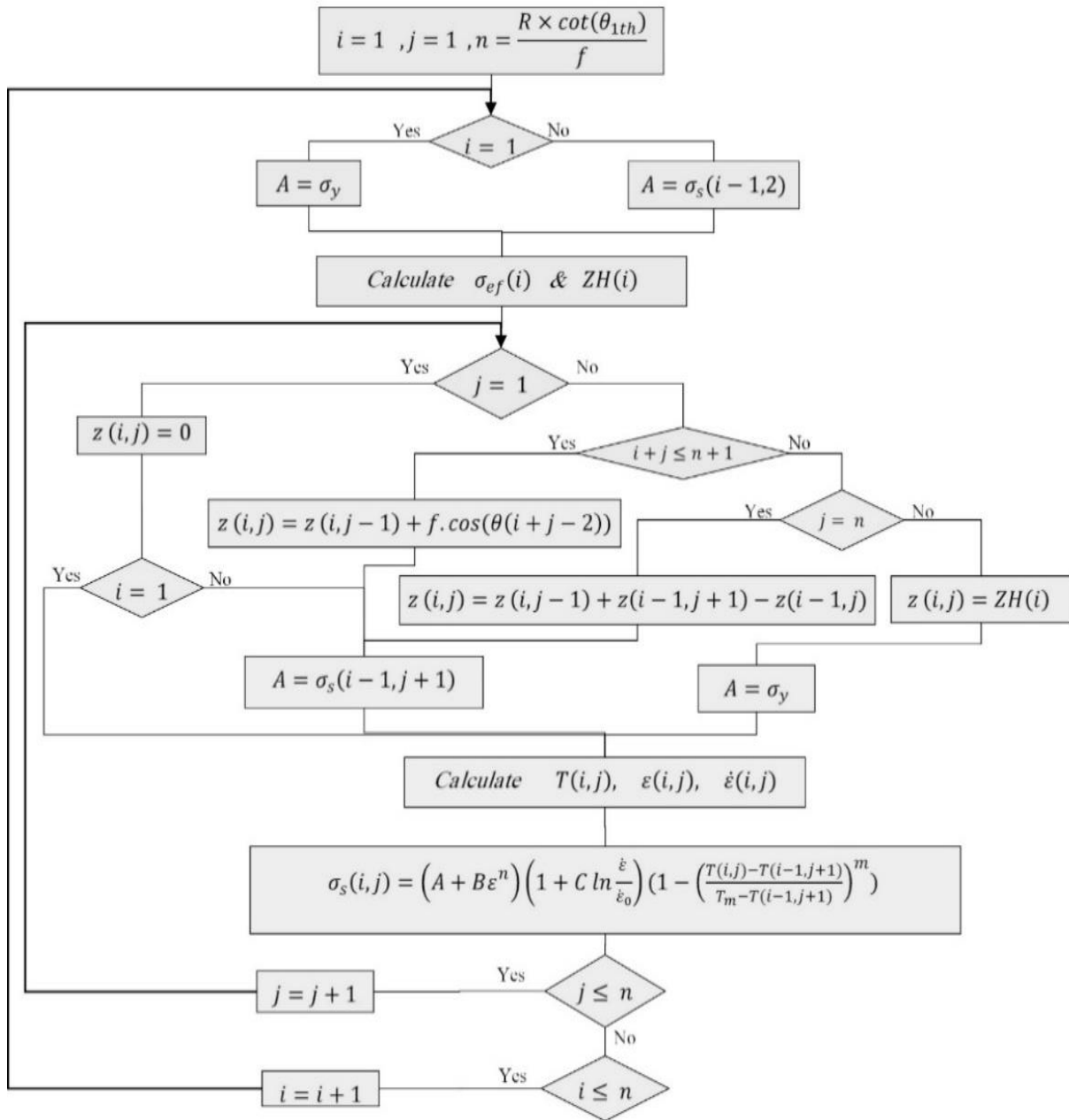


Fig.10 Strength curve calculating algorithm

4. Validating the proposed model and discussion

In this section, the hardness in the surface and subsurface layers of the workpiece is investigated by comparing the results predicted by the analytical model and those measured experimentally. The performance of

the proposed model is validated by comparing the results. First, the process conditions such as the workpiece, cutting tools and machining parameters are explained, then, the experimental settings for microhardness measurement are described, and the microhardness curves for the test samples from surface to depth are obtained. Finally, the microhardness values

predicted by the analytical model are compared with the experimental results.

4.1. Experiment set up

Side milling (orthogonal cutting) of 2205 duplex stainless steel is studied in this paper, the picture and schematic of the experimental setup are shown in Fig.12. As shown in this figure, the shear inserts are placed on the tool holder in a way that the insert cutting edge is parallel to the tool axis. The chemical composition and physical properties of this material are summarized in Table 1 and Table 2 and The Johnson–Cook material parameters of workpiece material are given in Table 3 [32].

Table 1. Chemical composition of duplex stainless steel 2205

C	Si	Mn	P	N	Cr	Mo	Ni	Cu	W	Co
0.016	0.48	1.31	0.02	0.17	22	3.16	5.6	0.16	0.02	0.09

Table 2. Physical properties of workpiece/tool materials.

Property	DSS 2205	Tpun160306 (uncoated cemented carbide)
Specific heat (J/kg°C)	418	200
Thermal conductivity ($W/m^{\circ}C$)	17	100
Density (kg/m ³)	7800	13800
Melting temperature °C	1460	

A milling insert holder with three Uncoated cemented carbide cutting tool inserts (Tpun160306 from Sandvik) are used in this study, the radius of milling insert holder is 15 mm and the cutting tool edge geometry is described in Table 4.

Table 3. Johnson-Cook material constants

A (MPa)	B (MPa)	n	C	m	$\dot{\epsilon}_0$ (1/s)
514	612.96	0.1801	0.0119	0.9765	1

Table 4. Cutting tool edge geometry

Designation	Rake angle (deg)	Clearance angle (deg)	Edge radius (μm)
TPUN160308	0	7	25

The physical characteristics of the insert were taken from the DEFORM software, (summarized in Table 2). Test blocks dimensions were 15×50×50mm, To have a uniform material that the surface layer be similar its bulk the side surfaces of the all blocks were ground and polished.

The performed experiments and Machining conditions listed in table 5. In these experiments, the cutting speeds and feed were varied in three levels, while the axial and radial depths of the cuts were constant.

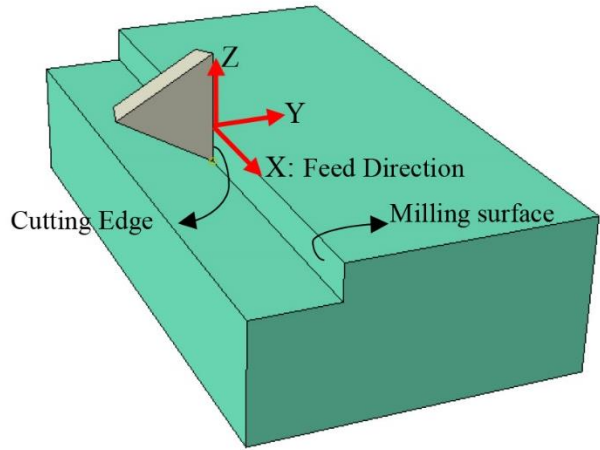
Table 5. experiments and Machining conditions

Run Order	Feed per tooth (μm)	Axial depth (mm)	Radial Depth (mm)	Speed (m/min)
1	80	3	7	75
2	160	3	7	23
3	50	3	7	37
4	160	3	7	37
5	50	3	7	75
6	80	3	7	23

To measure the hardness of the machined surface and subsurface layers, a Vickers indenter was used with a force of 0.02 kgf over 10s by a Qness 10A microhardness tester. The closest distance to the machined surface from the indentations was selected 15 μm . Besides, the minimum distance between two indentations was 30 μm . To obtain the hardness profile, the microhardness was measured at 7 points. The hardness test setup and pattern is illustrated in Fig. 12.



a)



b)

Fig.11 Experiment setup of milling a) picture and b) schematic

4.2. Validation

Using empirical Pawade's model, the linear relationship between the final strength and microhardness stress (Eq. 32), is used to predict the microhardness[33].

$$Hv = D \times \sigma_s \quad (32)$$

Where σ_s is the strength that calculated from algorithm shown in Fig.13. The coefficient correlating the hardness and yield stress (D) was estimated to be 0.439, which was obtained by least squares fit.

Fig. 13 shows the hardness curves from the measurement and prediction as well as the error between the two curves at each point. Fig. 13 present the comparisons between predicted and measured microhardness, considering the test error curves under different cutting conditions. It can be concluded that the model predicts the hardness with a good approximation. In Table 6, the Max and average error values are shown for each test.

Table 6. Maximum and average error values for each test

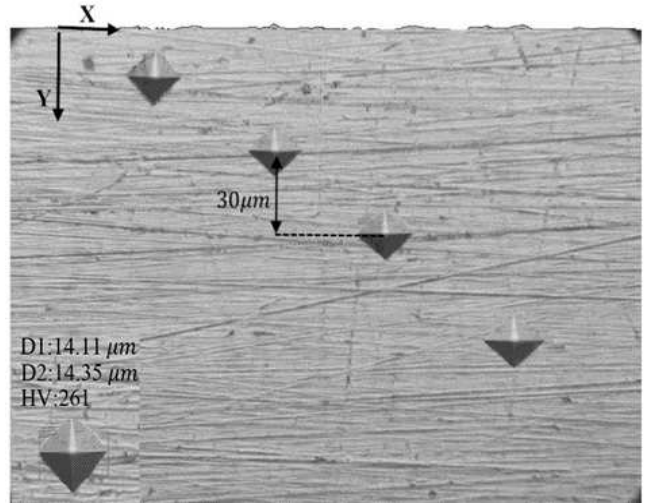
Test number.	1	2	3	4	5	6
Max Error (%)	15	15	14	7	8	7
Average Error (%)	8	7	11	4	4	3

5. Conclusion

This study presented a theoretical model to evaluate work hardening in the milling process of duplex stainless steel. The model was implemented by programming in MATLAB software. The comparison of experimental and theoretical results indicates that the model can well predict work hardening. Work hardening is more significant on the surface of the workpiece compared to the deeper regions since the layers closer to the surface are more deformed. By going deeper into the workpiece, the hardness decreases until it reaches the initial hardness of the workpiece material. For the same cutting speed, the strain hardening increases by increasing feed rate. The increase of cutting speed has less effect on strain hardening. This is because although an increase in shear velocity increases strain rate, it also increases the temperature in the cutting region. Therefore, these interacting factors can reduce the effect of cutting speed on strain hardening.

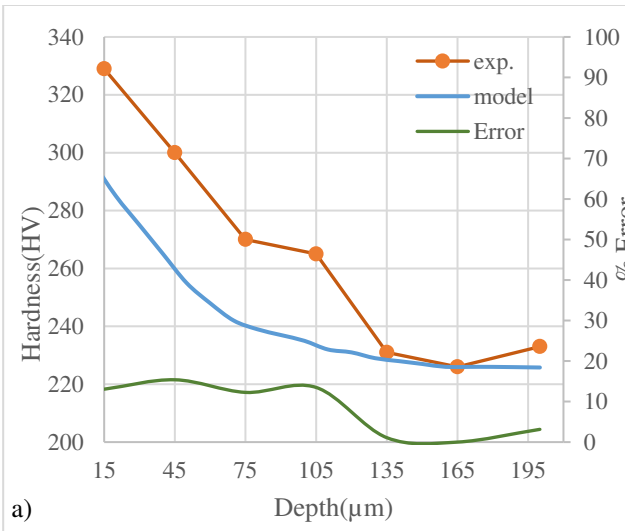


a)

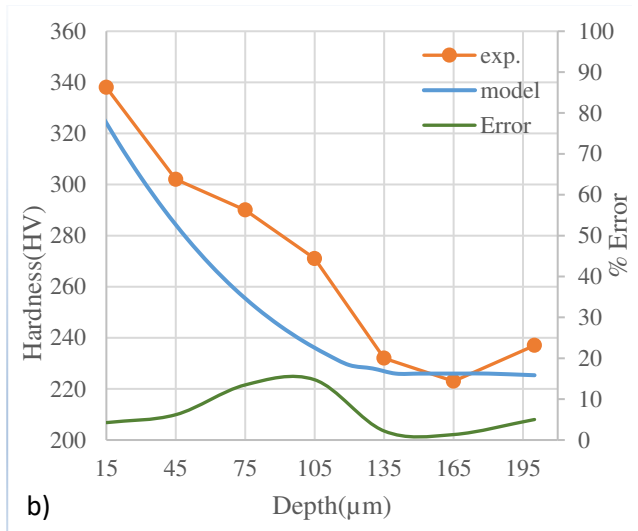


b)

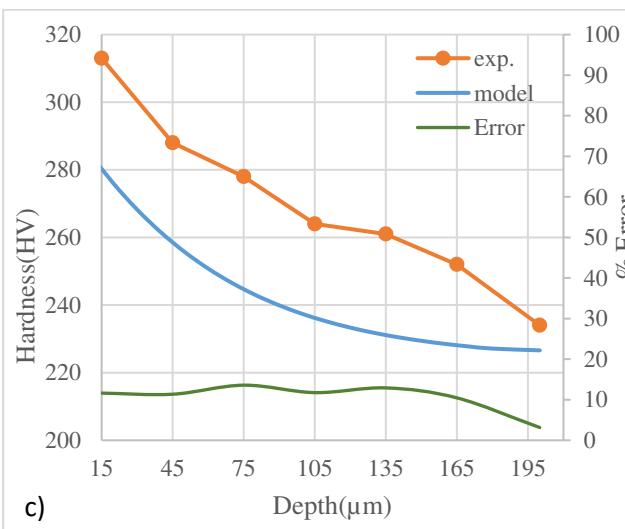
Fig.12 a)The hardness test setup b) The hardness test pattern.



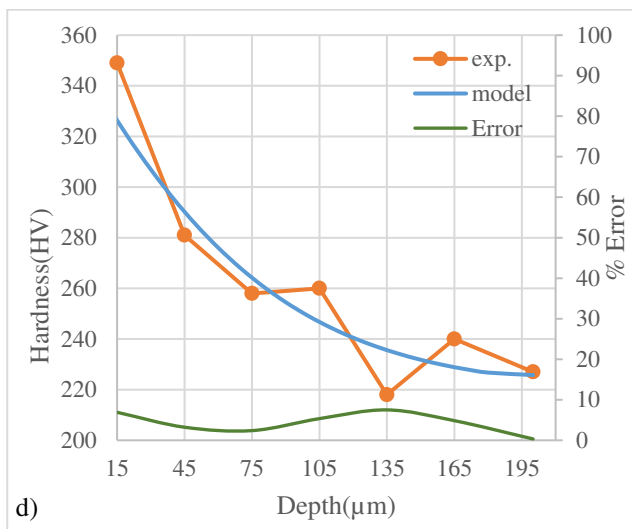
a)



b)



c)



d)

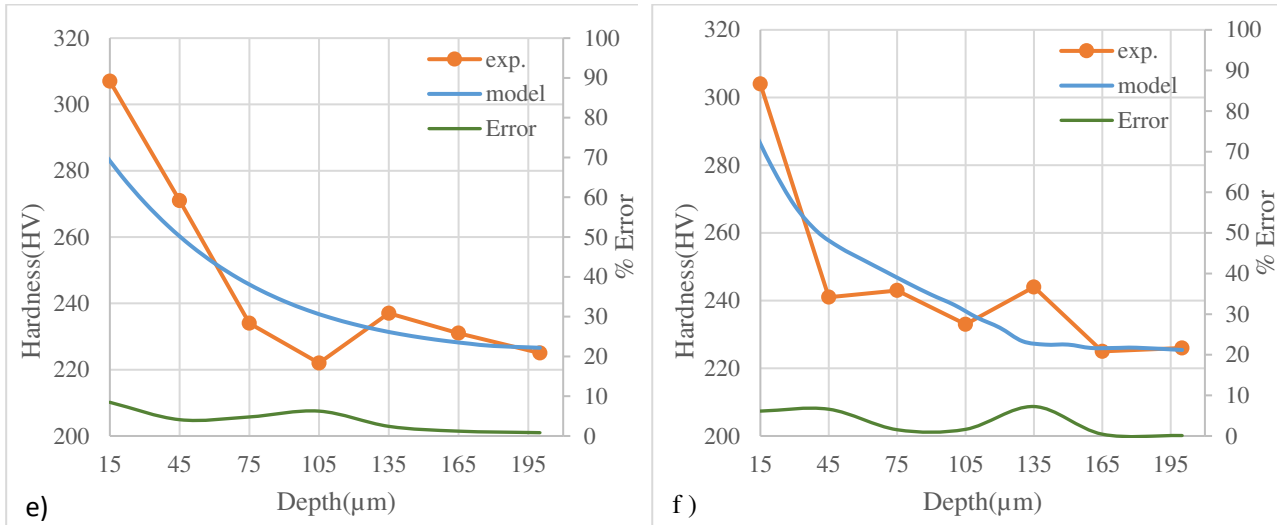


Fig. 13 Comparisons of subsurface microhardness obtained by analytical model and experimental tests: (a)–(f) correspond to cutting conditions from 1 to 6 (in table 6), respectively



Declarations

Authors' contributions

Y. Mohammadi: Conceptualization, methodology, investigation, analysis, writing-original draft.

H. Amirabadi: Conceptualization, methodology, Supervision, writing-review & editing.



Conflicts of interest, The authors declare that there is no conflict of interest in this work.

Funding, This research did not receive any specific grant from funding agencies in the public, commercial or not for profit sector.

Ethical approval, This article does not contain any studies with human participants or animals performed by any of the authors

Yousef Mohammedi received his B.Sc. in mechanical engineering from SRU in 2008, and his M.Sc. in manufacturing engineering from AUT in 2011. He is currently a Ph.D. student in mechanical engineering at University of Birjand, Iran. His research interests include cutting process, surface integrity machining modeling.

Hossein Amirabadi received his B.Sc. in mechanical engineering from Ferdowsi University in 1998, and his M.Sc. in manufacturing engineering from IUT

University in 2002. He received his Ph.D. in manufacturing engineering from University of Mazandaran in 2006. He is currently an associate Prof. at University of Neyshabur, Iran. His research interests include metal cutting, machining simulation, surface finishing, metrology and CAD/CAM.

Reference.

1. Stephenson DA, Agapiou JS (1997) Metal Cutting Theory and Practice Manufacturing.
2. DeGarmo EP, Black JT, Kohser RA, Klamecki BE (1997) Materials and process in manufacturing: Prentice Hall Upper Saddle River.
3. Birger I (1984) Using multidimensional strength criteria for determining the probability of failure. Strength of Materials 16(11):1520-5.
4. Savkin A (2007) Assessing the reliability of thread joints under variable loads. Journal of Machinery Manufacture and Reliability 36(4):336-40.
5. Childs T (2009) Modelling orthogonal machining of carbon steels. Part I: strain hardening and yield delay effects. International Journal of Mechanical Sciences 51(5): 402-411.
6. Fetullazade E, Akyildiz H.K, Saritas S (2010) Effects of the machining conditions on the strain hardening and the residual stresses at the roots of screw threads. Materials & Design 31(4): 2025-2031.
7. Thakur D.G, Ramamoorthy B, Vijayaraghavan L (2012) Effect of cutting parameters on the degree of work hardening and tool life during high-speed machining of Inconel 718. The International Journal of Advanced Manufacturing Technology 59(5): 483-489.

8. Krolczyk G, Legutko S, Stoić A (2013) Influence of cutting parameters and conditions onto surface hardness of duplex stainless steel after turning process. *Tehnički vjesnik* 20(6): 077-1080.
9. Ren X, Liu Z (2016) Influence of cutting parameters on work hardening behavior of surface layer during turning superalloy Inconel 718. *The International Journal of Advanced Manufacturing Technology* 86(5): 2319-2327.
10. Hua Y, Liu Z (2018) Effects of cutting parameters and tool nose radius on surface roughness and work hardening during dry turning Inconel 718. *The International Journal of Advanced Manufacturing Technology* 96(5): 2421-2430.
11. Wang G (2018) Effect of cutting parameters on strain hardening of nickel–titanium shape memory alloy. *Smart Materials and Structures* 27(7): 075027.
12. Wang G (2019) Influence of cutting parameters on surface roughness and strain hardening during milling NiTi shape memory alloy. *The International Journal of Advanced Manufacturing Technology* 102(5): 2211-2221.
13. Shaw MC, Cookson J (2005) *Metal cutting principles*: Oxford university press New York.
14. Wang S.Y, Yang W.J, Ma L.L (2012) Advances in Theoretical Investigation of Work Hardening for Metal Cutting. in *Applied Mechanics and Materials*. Trans Tech Publ.
15. Olsson M, Bushlya V, Zhou J, Ståhl J-E (2016) Effect of feed on sub-surface deformation and yield strength of oxygen-free pitch copper in machining. *Procedia CIRP* 45:103-6.
16. Bailey J, Jeelani S (1976) Determination of subsurface plastic strain in machining using an embossed grid. *Wear* 36(2):199-206.
17. Ghadbeigi H, Bradbury S, Pinna C, Yates J (2008) Determination of micro-scale plastic strain caused by orthogonal cutting. *International Journal of Machine Tools and Manufacture* 48(2):228-35.
18. Guo Y, M'Saoubi R, Chandrasekar S (2011) Control of deformation levels on machined surfaces. *CIRP annals* 60(1):137-40.
19. Liang S, Su J-C (2007) Residual stress modeling in orthogonal machining. *CIRP annals* 56(1):65-8.
20. Oxley PLB(1989) *The mechanics of machining: an analytical approach to assessing machinability*: Ellis Horwood.
21. Fang N (2003) Slip-line modeling of machining with a rounded-edge tool—Part I: new model and theory. *Journal of the Mechanics and Physics of Solids* 51(4):715-42.
22. Fang N (2003) Slip-line modeling of machining with a rounded-edge tool—Part II: analysis of the size effect and the shear strain-rate. *Journal of the Mechanics and Physics of Solids* 51(4):743-62.
23. Lalwani D, Mehta N, Jain P (2009) Extension of Oxley's predictive machining theory for Johnson and Cook flow stress model. *Journal of materials processing technology* 209(12-13):5305-12.
24. Grzesik W (2008) *Advanced machining processes of metallic materials: theory, modelling and applications*: Elsevier.
25. Zhang D, Zhang X-M, Leopold J, Ding H (2017) Subsurface deformation generated by orthogonal cutting: analytical modeling and experimental verification. *Journal of Manufacturing Science and Engineering* 139(9).
26. Pawlik PS (1980) Reisman H. *Elasticity: theory and applications*: Wiley.
27. Johnson K (1985) *Contact mechanics*", Cambridge University Press, New York, USA.
28. Hahn RS (1951) editor *On the temperature developed at the shear plane in the metalcutting process*. *Journal of Applied Mechanics-Transactions of the ASME*
29. Komanduri R, Hou Z.B (2001) Thermal modeling of the metal cutting process—Part II: temperature rise distribution due to frictional heat source at the tool–chip interface. *International Journal of Mechanical Sciences* 43(1): 57-88.
30. Karas A, Bouzit M, Belarbi M (2013) Development of a thermal model in the metal cutting process for prediction of temperature distributions at the tool–chip–workpiece interface. *Journal of theoretical and applied mechanics* 51(3): p. 553--567.
31. Shen S, Atluri S (2006) An analytical model for shot-peening induced residual stresses. *Computers, Materials and Continua* 4(2):75-85.
32. Koyee RD, Schmauder S, Heisel U, Eisseler R. (2015) Numerical modeling and optimization of machining duplex stainless steels. *Production & Manufacturing Research* 3(1):36-83.
33. Pawade R, Joshi SS, Brahankar P.(2008) Effect of machining parameters and cutting edge geometry on surface integrity of high-speed turned Inconel 718. *International Journal of Machine Tools and Manufacture* 48(1):15-28.

Figure 2

a) Geometric model of cutting zones and b) details of slip-line model in the tertiary shear zone [22].

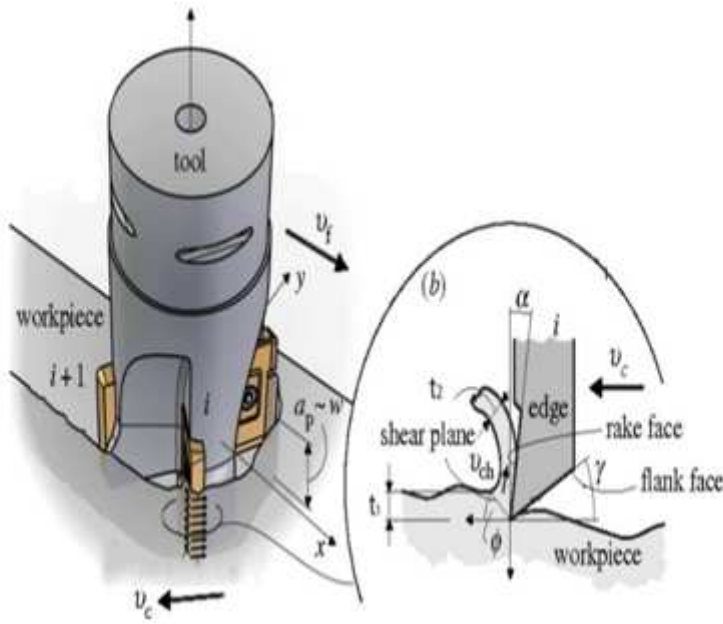


Figure 3

Geometric parameters of orthogonal cutting in milling.

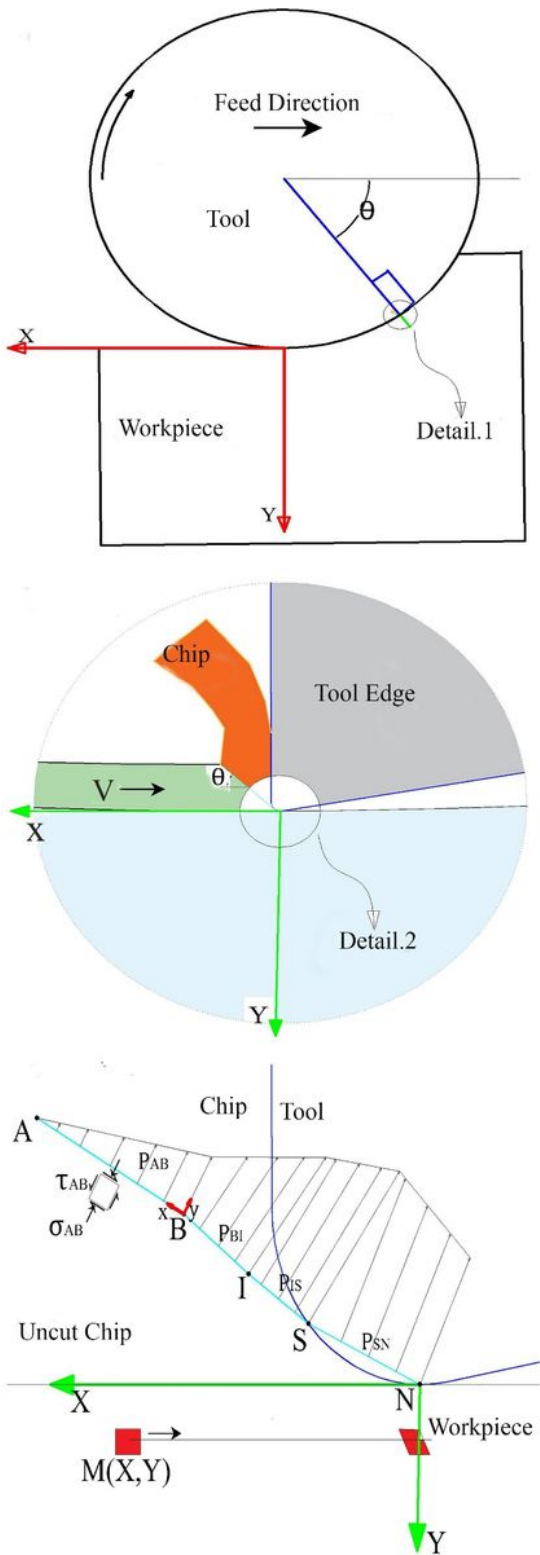


Figure 4

a) An overall view of tool and workpiece and their relative motion, b) Details of interface between cutting edge and workpiece c) details of the cutting zone around the cutting edge and the slip-line model.

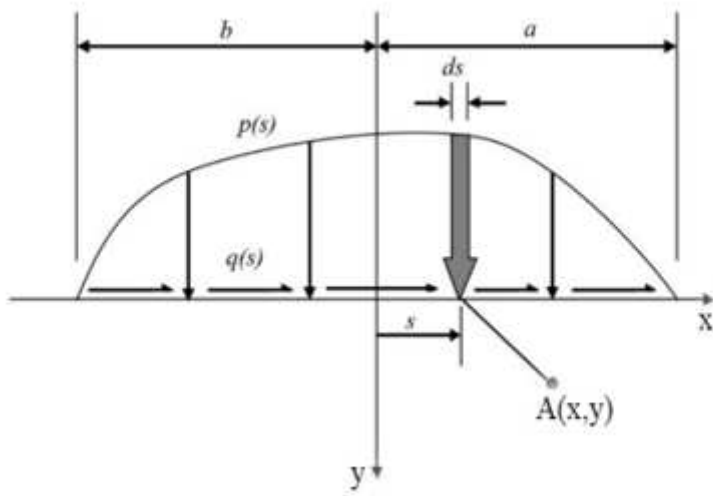


Figure 5

Boundary conditions for Boussinesq equations [27]

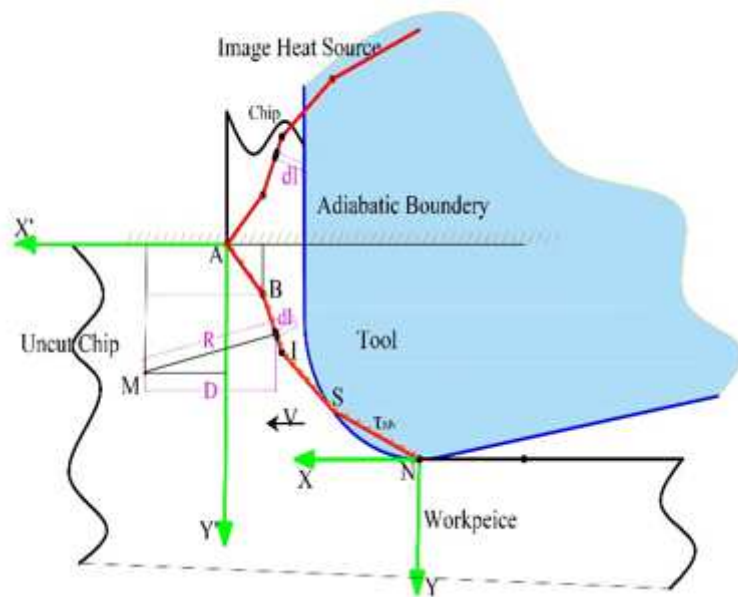


Figure 6

Heat sources and coordinate axes for calculating temperature.

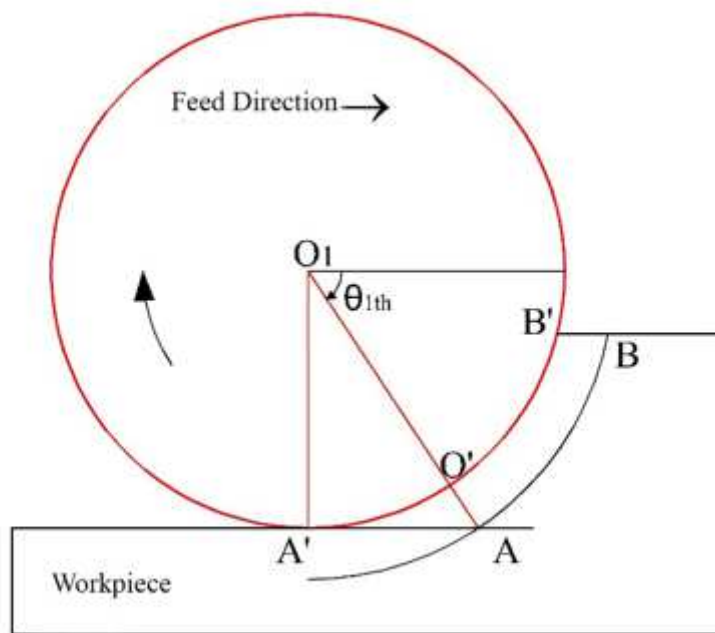
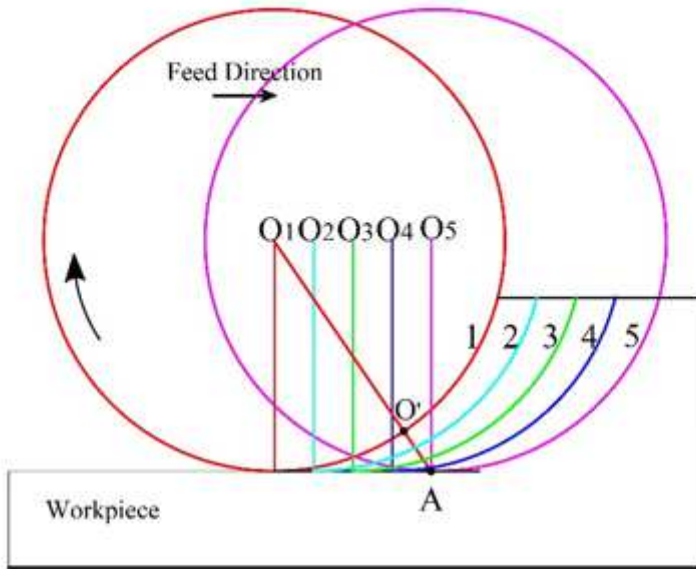
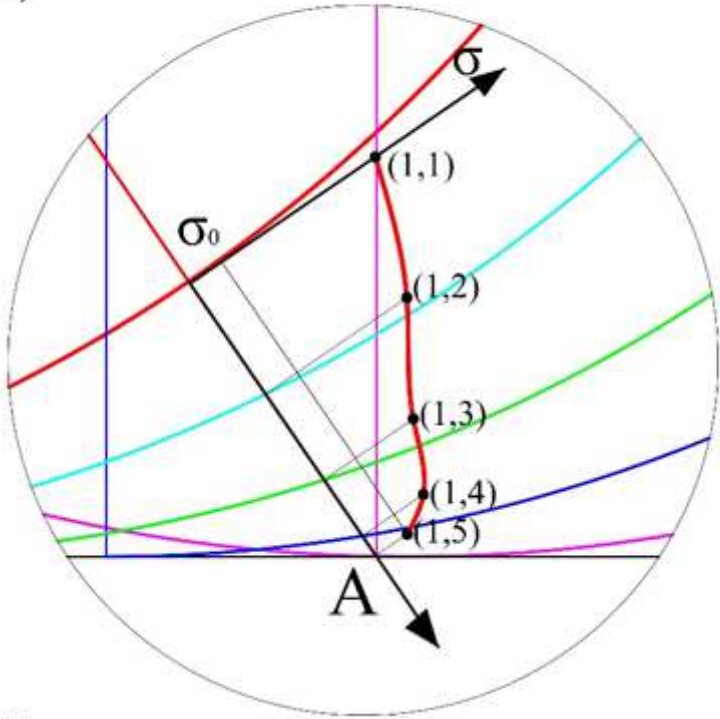


Figure 7

Tool-workpiece engagement and the penetration depth profile of work hardening.



a)



b)

Figure 8

Cutting paths for a workpiece surface under 5 times deformation and b) details of the edge tip and strength curve.

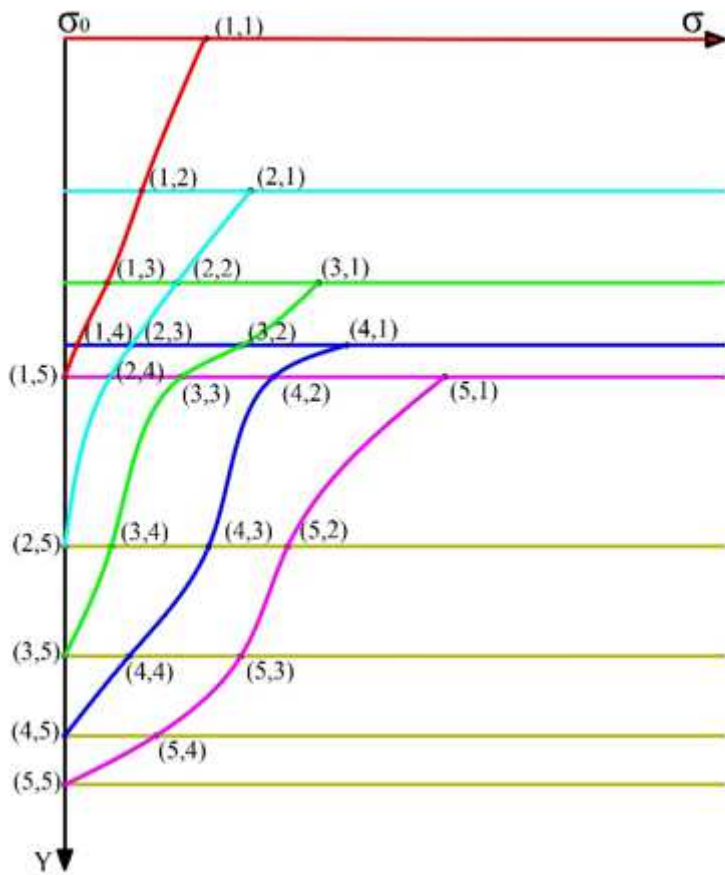


Figure 9

Schematic of strength curves for cutting paths has been shown in Fig. 8.

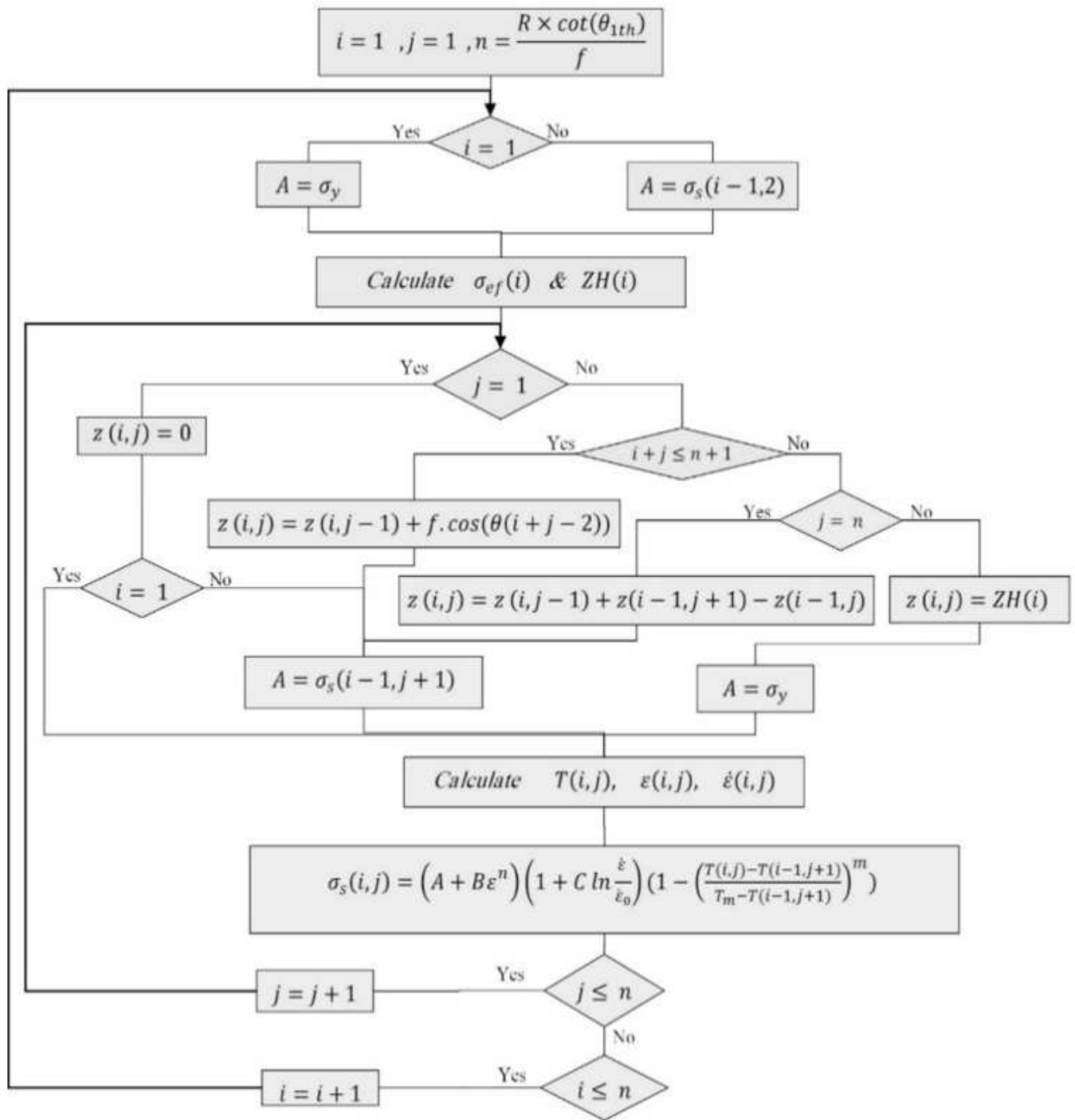
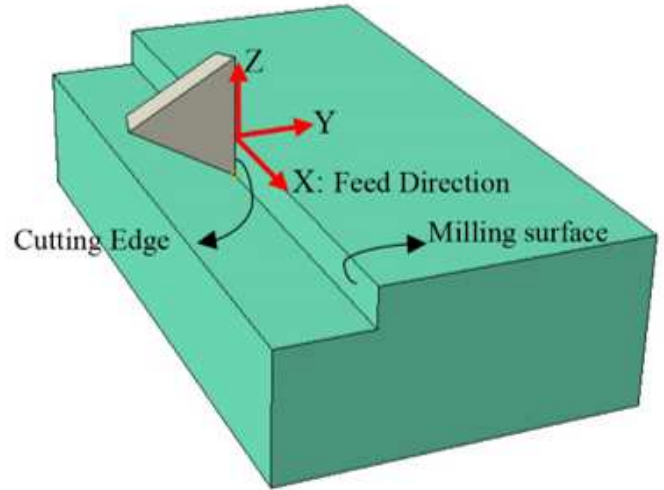


Figure 10

Strength curve calculating algorithm



a)



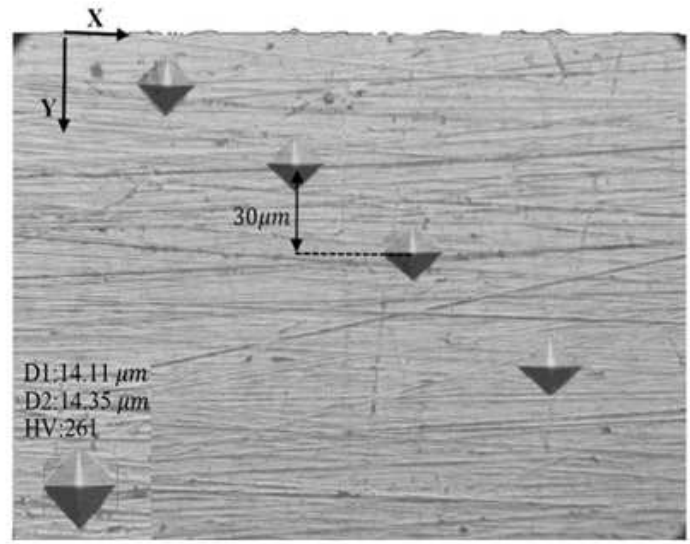
b)

Figure 11

Experiment setup of milling a) picture and b) schematic



a)



b)

Figure 12

a) The hardness test setup b) The hardness test pattern.

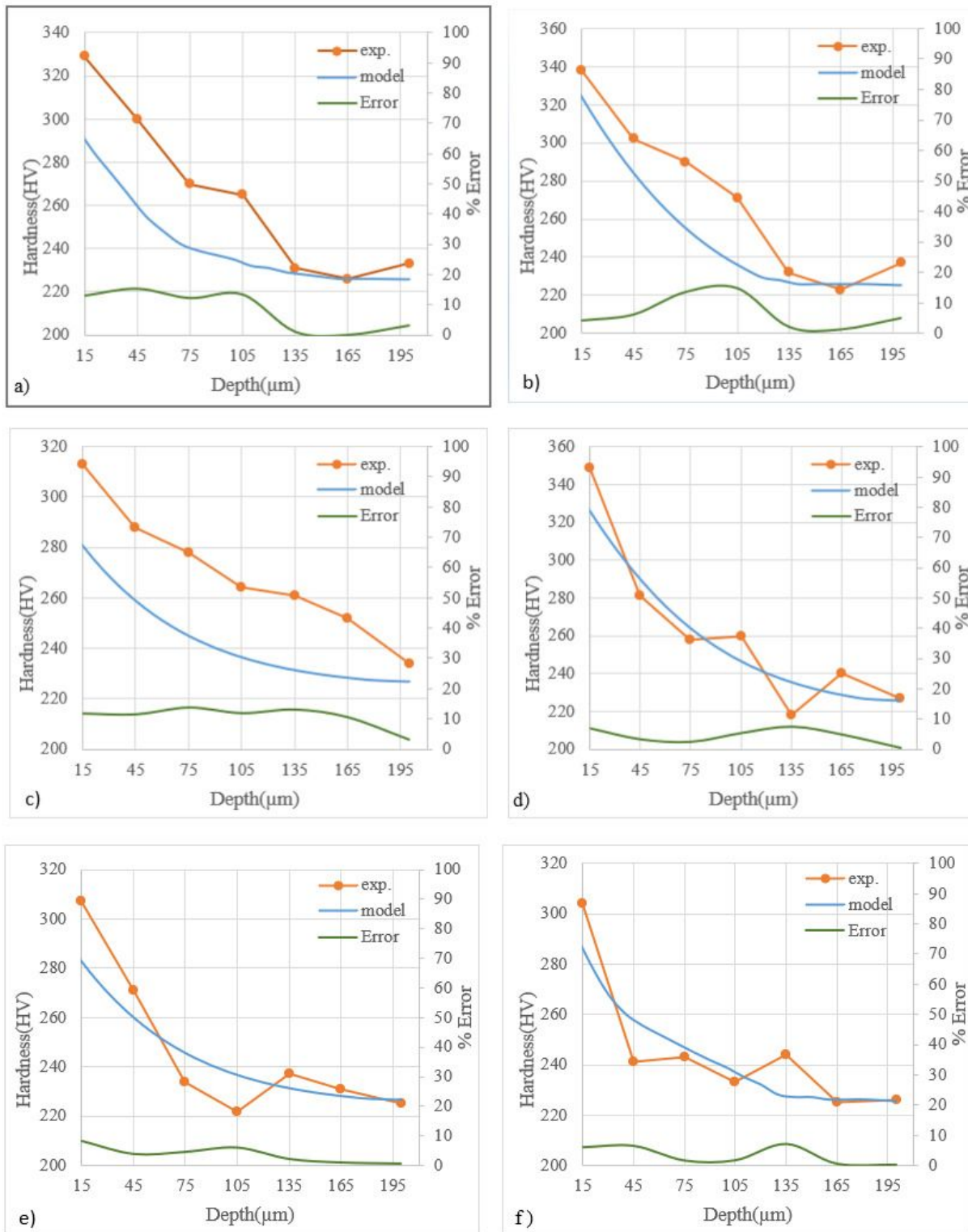


Figure 13

Comparisons of subsurface microhardness obtained by analytical model and experimental tests: (a)–(f) correspond to cutting conditions from 1 to 6 (in table 6), respectively